npj Computational Materials

www.nature.com/npjcompumats

ARTICLE OPEN

Origin of ultrafast growth of monolayer WSe_2 via chemical vapor deposition

Shuai Chen[1], Junfeng Gao[1,2], Bharathi M. Srinivasan[1], Gang Zhang[1], Viacheslav Sorkin[1], Ramanarayan Hariharaputran[1] and Yong-Wei Zhang[1]

The ultrafast growth of large-area, high-quality WSe_2 domains with a compact triangular morphology has recently been achieved on a gold substrate via chemical vapor deposition. However, the underlying mechanism responsible for ultrafast growth remains elusive. Here, we first analyze growth processes and identify two possible pathways that might achieve ultrafast growth: Path 1, fast edge attachment and ultrafast edge diffusion; Path 2, fast kink nucleation and ultrafast kink propagation. We perform kinetic Monte Carlo simulations and first-principles calculations to assess the viability of these two paths, finding that Path 1 is not viable due to the high edge diffusion barrier calculated from first-principles calculations. Remarkably, Path 2 reproduces all the experimental growth features (domain morphology, domain orientation, and growth rate), and the associated energetic data are consistent with first-principles calculations. The present work unveils the underlying mechanism for the ultrafast growth of WSe_2, and may provide a new route for the ultrafast growth of other two-dimensional materials.

npj Computational Materials (2019)5:28 ; https://doi.org/10.1038/s41524-019-0167-2

INTRODUCTION

Two-dimensional (2D) materials, such as graphene, boronitrene, phosphorene, transition metal dichalcogenides (TMDs), have attracted a great deal of attention due to their fascinating lattice structures and electronic properties.[1–4] WSe_2, a member in the TMD family, is a semiconducting material with a sizable band gap, high charge mobility, high on–off ratio, and tunable electronic and optical properties.[5–7] For example, bulk WSe_2 is a p-type semiconductor with an indirect band gap of ~1.2 eV, while monolayer WSe_2 exhibits a direct band gap of ~1.65 eV.[8] In addition, an indirect to direct band gap transition can be achieved in WSe_2 by strain.[9] In particular, the carrier mobility in WSe_2 recently obtained by epitaxy growth is up to 143 $cm^2/(V\,s)$,[10] which is remarkably higher than that in other TMDs.[11–13] Therefore, WSe_2 is a promising semiconducting 2D material suitable for ultrafast electronics and optoelectronics.

To realize such applications, fast and mass synthesis of large-area, high-quality 2D WSe_2 is essential. Synthesis of 2D WSe_2 can be achieved by mechanical exfoliation,[14,15] liquid exfoliation,[16–18] and chemical vapor deposition (CVD).[10–13] Among them, CVD has the advantage of the controllable growth of large-area 2D TMDs with the specific lattice structures and the targeted number of layers.[10–13,19,20] Besides that, CVD is also convenient for synthesizing intra-layer junctions between various 2D TMDs, which may have novel applications in electronics and optoelectronics.[21,22]

One of the challenges in the CVD growth of 2D TMDs is the low growth rate.[19–26] It was shown that even by increasing the feedstock concentration or using a gas-phase promoter, the growth rate was still low, often <0.5 μm/s on nonmetal substrates.[25,26] This is in sharp contrast to graphene, whose growth rate can reach up to 60 μm/s on Cu foil with the assistance of oxygen atoms.[27–29] Artyukhov et al.[30] proposed that the growth rate of graphene was mainly determined by the kink nucleation because the kink nucleation had a considerable energy barrier to overcome while the kink propagation only had a small energy barrier (which might even fully vanish if the feedstock and catalyst provide carbon in the dimer form). A similar kink-nucleation-propagation mechanism was also revealed in the growth of hexagonal boron nitride.[31] Since chalcogenide atoms are able to etch metal substrates, few metal surfaces are suitable for the epitaxial growth of TMDs. Although Au surfaces were used to grow monolayer MoS_2,[11,32] and WS_2,[12,13] the growth rates were generally low (<0.7 μm/s). Recently, a surprising breakthrough has been made by Gao et al.[10] in the growth of monolayer WSe_2 on Au (111) by CVD. Remarkably, they have been able to achieve ultrafast growth rates of ~8.3 μm/s at 800 °C and ~26 μm/s at 950 °C. In addition, the grown WSe_2 domains took a regular triangular shape with compact edges, and most importantly, they were of high quality. These features are distinctively different from other 2D materials with similar CVD growth conditions.[27–29]

We note that significant theoretical efforts have been made to understand the growth of graphene.[27–30,33–45] However, only a few theoretical studies have been performed to understand the growth behavior of TMDs due to their complex compound structures.[46–52] Recently, kinetic Monte Carlo (kMC) simulations have also been employed to examine the growth processes of TMDs.[50–52] However, the growth rates that were obtained for compact triangular domains at 1273 K (~10^{-6} μm/s,[50] ~10^{-5} μm/s,[51] ~10^{-4} μm/s[52]) were much lower than that obtained by Gao et al.[10] (26 μm/s). So far, the underlying growth mechanism for the ultrafast growth of regular triangular WSe_2 domains with compact edges remains elusive.

[1]Institute of High Performance Computing, A*STAR, Singapore 138632, Singapore and [2]Key Laboratory of Materials Modification by Laser, Ion and Electron Beams, Dalian University of Technology, Ministry of Education, Dalian 116024, People's Republic of China
Correspondence: Yong-Wei Zhang (zhangyw@ihpc.a-star.edu.sg)
These authors contributed equally: Shuai Chen, Junfeng Gao

Received: 31 July 2018 Accepted: 12 February 2019
Published online: 27 February 2019

Published in partnership with the Shanghai Institute of Ceramics of the Chinese Academy of Sciences

npj nature partner journals

In this work, we aim to unveil the origin of the ultrafast growth of triangular WSe_2 domains with compact edges on Au surface by combining first-principles calculations and kMC simulations. First, we analyze the growth processes and identify possible paths that are potentially viable to realize the ultrafast growth. Our analysis shows that there are two possible paths, that is, Path 1: fast edge attachment and ultrafast edge diffusion, and Path 2: fast kink nucleation and ultrafast kink propagation along the edge. Our results show that Path 1 is not viable due to the high diffusion energy barrier along the edges calculated from our first-principles calculations. For Path 2, however, our kMC simulation results for the growth morphology and growth rate for a wide range of deposition fluxes and temperatures agree well with the experiments. In addition, the used energetic data are consistent with first-principles calculation results. Hence, our study here not only unveils the origin of the ultrafast growth mechanism for WSe_2, but also potentially presents a novel route to achieve ultrafast growth of other TMDs with large size, compact shape, and high quality.

In Gao et al. experiment,[10] atomic force microscopy measurements showed that the WSe_2 domain had a uniform thickness of ~0.75 nm and average surface roughness of ~0.3 nm. The small roughness was due to the different thermal coefficient between WSe_2 and Au. Moreover, the Raman spectra taken from 20 random positions showed the same feature in terms of peak position and intensity. All these results indicated that the ultrafast grown WSe_2 domains on Au were uniform monolayers. Based on these experimental observations, we constructed our 2D model to unveil the underlying mechanism on the ultrafast growth of monolayer. The following six dominant events are considered (see the schematic in Fig. 1): (1) deposition of atoms to substrate surface (surface deposition, F), (2) deposition of atoms at domain edge (edge deposition, F'), (3) diffusion of adatoms on substrate surface (surface diffusion, E_{di}), (4) attachment of adatoms to domain edge (attachment, E_{at}), (5) detachment from domain edge (detachment, E_{de}), and (6) diffusion of atoms along domain edge (edge diffusion, E_{ed}). It is well-known that the domain morphology and growth rate are primarily governed by the rates of surface diffusion (r_{di}), attachment (r_{at}), and edge diffusion (r_{ed}), which are in turn determined by their energetics (E_{di}, E_{at}, E_{de}, E_{ed})[37] and the growth parameters (F, F', T),[42] where T is the growth temperature. A diagram classifying the growth conditions of WSe_2 based on their occurrence rates is shown in Fig. 2a. A key factor that

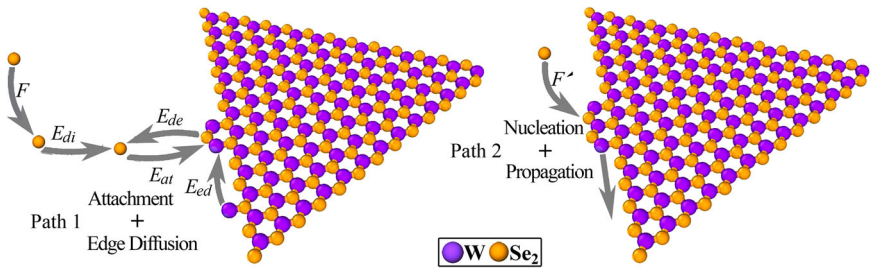

Fig. 1 Schematic of the two possible paths for the ultrafast growth of triangular WSe_2 domains. The purple and orange spheres denote W and Se atoms, respectively. F and F' represent the deposition fluxes for the surface deposition and edge deposition, correspondingly. E_{di}, E_{at}, E_{de}, and E_{ed} represent the energy barriers for the surface diffusion, attachment, detachment, and edge diffusion processes, respectively. Path 1: fast attachment and ultrafast edge diffusion (left panel), and Path 2: fast kink nucleation and ultrafast kink nucleation (right panel)

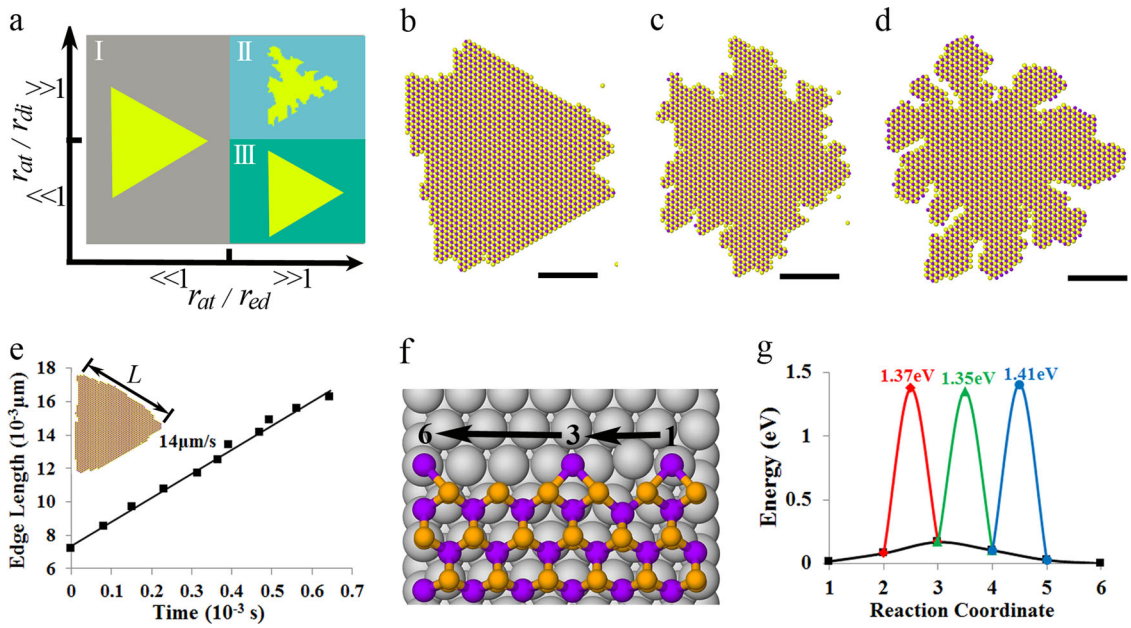

Fig. 2 **a** Diagram classifying the growth conditions based on the different ratio of attachment rate (r_{at}) to the edge diffusion rate (r_{ed}) and to the surface diffusion rate (r_{di}). Domain morphologies at 800 °C with **b** $E_{ed} = 0.5$ eV, **c** $E_{ed} = 1.0$ eV, and **d** $E_{ed} = 1.5$ eV, respectively, at $F_S = 2.0 \times 10^{-2}$ ML/s and $F_W = 1.8 \times 10^{-2}$ ML/s. **b**–**d** Scale bar: $10a$ ($a = 0.332$ nm). **e** Growth rate of the edge length as a function of time at 800 °C with $E_{ed} = 0.5$ eV. **f** Schematic illustration of the six energetically favorable sites for in-plane diffusion of W atom along the Se-terminated zigzag edge. Purple, orange, and gray spheres represent W, Se, and Au atoms, respectively. **g** The energy barriers for edge diffusion obtained from first-principles calculations: red: site 2 to site 3, green: site 3 to site 4, and blue: site 4 to site 5

controls the domain morphology is the relative dominance between attachment rate (r_{at}) and edge diffusion rate (r_{ed}). When $r_{at}/r_{ed} \ll 1$, the domain grows in the thermodynamic regime, in which a regular triangular shape with low-energy edges can be maintained due to the fast edge diffusion rate and relatively low attachment rate. Hence, it is possible to achieve the ultrafast growth of WSe_2 domain with a regular triangular shape by a fast attachment rate and an even faster edge diffusion rate (i.e., Path 1 as shown in Fig. 1).

When $r_{at}/r_{ed} \gg 1$, the domain grows in the kinetic regime, in which the domain morphology is governed by r_{at}/r_{di}, where r_{di} is the surface diffusion rate. When $r_{at}/r_{di} \ll 1$, the fast surface diffusion rate is able to assist the attachment of adatoms to the most energetically favorable sites. In this scenario, a complete compact shape could also be achieved. Both the fast kink nucleation and propagation could be completed quickly by the fast attachment of adatoms from substrate or vapor. Clearly, if the kink nucleation rate is fast and the kink propagation is even faster along the edges, it is also possible to achieve the ultrafast growth of WSe_2 domain with a regular triangular shape (i.e., Path 2 as shown in Fig. 1). This mechanism has been proposed to explain the growth of graphene[30] and hexagonal boron nitride.[31] When $r_{at}/r_{di} \gg 1$, however, the growth is in the diffusion-limited regime, in which the domain morphology becomes dendrite or fractal. In this regime, it is not possible to achieve the regular triangular shape. The term "ultrafast" was proposed in Gao et al. experimental work.[10] In their work, they achieved a growth rate of 26 μm/s, which was 2–3 orders of magnitude faster than previous studies.[19–26] To achieve this ultrafast growth rate of 26 μm/s, together with triangular domains with compact edges, the edge attachment to form kink should be fast. In addition, the edge diffusion to the kink or kink propagation should be even faster. Based on our first-principles calculations and kMC simulations, we are able to give more quantitative descriptions to terms "fast" and "ultrafast": If the energy barrier for an event is ~0.5 eV (for example, the kink formation with an energy barrier of 0.55 eV), we call it "fast". On the other hand, if the energy barrier for an event is much lower than 0.5 eV (for example, the surface diffusion of adatom with an energy barrier of 0.36 eV), we call it "ultrafast".

Our above analyses of growth mechanisms suggest two possible paths that are able to achieve the ultrafast growth of WSe_2 domain with a regular triangular shape, that is, Path 1: a fast attachment and an ultrafast edge diffusion along the domain edges, and Path 2: a fast kink nucleation and an ultrafast kink propagation rate along the domain edges. These two paths are schematically illustrated in Fig. 1. In the following, we perform first-principles calculations and kMC simulations to assess the viability of the two possible paths.

RESULTS

Path 1: fast attachment and ultrafast edge diffusion

To find out the deposition flux for Se dimer (F_S) and W atom (F_W) corresponding to Gao et al.[10] experimental growth conditions, we performed a sequence of kMC simulations by varying F_S and F_W. We found that when $F_S = 2.0 \times 10^{-2}$ and $F_W = 1.8 \times 10^{-2}$ ML/s, the growth rate of the WSe_2 domain is ~14 μm/s (c.f. Fig. 2e), which is consistent with that obtained by Gao et al.[10] (8.3–26 μm/s). The kMC simulated domain morphologies at three different energy barriers for edge diffusion, that is, $E_{ed} = 0.5$, 1.0, and 1.5 eV are shown in Fig. 2b–d, respectively, with the same flux and coverage. Their morphological evolutions are shown in Supplementary Movies 1–3. It is seen that a compact triangular shape is achieved when $E_{ed} = 0.5$ eV (c.f. Fig. 2b) due to the fast diffusion of attached atoms capable to reach the global energetically favorable sites along the edges, which is also evidenced by the evolution of the domain morphology shown in Supplementary Movie 1. With increasing energy barrier for edge diffusion, however, the domain morphology becomes gradually more dendritic and fractal. This trend is clearly seen from Fig. 2c, d, and Supplementary Movies 2–3. The underlying reason for the trend is that when the energy barrier for the edge diffusion increases, for example, to 1.0 eV, the edge diffusion of the attached atoms is limited and they can only diffuse to local energetically favorable sites, leading to the rough edge morphologies. When the edge diffusion barrier is further increased to 1.5 eV, diffusion of the attached atoms to the energetically favorable sites becomes even less probable, resulting in a dendritic and fractal shape, which falls into the kinetic regime. Clearly, by increasing the diffusion energy barrier along the edges, there is a transition in the growth mode from the thermodynamic regime (compact triangular shape) to the kinetic regime (dendritic and fractal shape).

Our above kMC simulations clearly showed that Path 1 is able to achieve a triangular WSe_2 domain with ultrafast growth rate under the condition that the energy barrier for the edge diffusion must be low (≤0.5 eV). To validate this necessary condition, we performed first-principles calculations on the energy barriers of edge diffusion. First, we calculated the energies of W atom via different in-plane sites (marked by 1–6 in Fig. 2f) and out-of-plane sites (marked by I and II in Figure S3b in Supplementary Information) along the Se-terminated zigzag edge. Figure 2g shows the energies of W atom at the six in-plane steps. It is seen that the diffusion of W atom from site 1 to site 2 or from site 5 to 6 is easier than that from site 2 to site 3, site 3 to site 4, and site 4 to site 5 due to the lower energies of site 1 and site 6 (c.f. black squares in Fig. 2g). Therefore, the diffusion of W atom from site 2 to site 3 (c.f. red curve in Fig. 2g), site 3 to site 4 (c.f. green curve in Fig. 2g), and site 4 to site 5 (c.f. blue curve in Fig. 2g) were further calculated to obtain their diffusion energy barriers. It is seen from Fig. 2g that the energy barriers for the edge diffusion of W along Se-terminated edge are ~1.4 eV, which is significantly higher than 0.5 eV. We have also evaluated the energy barrier for Se atom diffusion along the W-terminated zigzag edge by first-principles calculations. We found that the W-terminated zigzag edge underwent reconstruction (c.f. Figure S3d), exhibiting substantial inward displacements of all the first-row W atoms and outward displacements of half of the second-row Se atoms. The same edge reconstruction has also been reported by Cui et al.[53] The minimum energy path for the diffusion of a Se atom along the reconstructed W-terminated zigzag edge is plotted in Figure S3e, and the schematic structures corresponding to the different states are shown in Figure S3f. The forward (from IS to FS in Figure S3f) diffusion barrier is 1.08 eV, while the backward one (from FS to IS in Figure S3f) is 2.94 eV, indicating the high energy barriers for Se diffusion along the reconstructed W-terminated zigzag edge. Such high energy barriers for the edge diffusion of both W and Se suggest that Path 1 is not energetically favorable and thus cannot be the underlying mechanism for the ultrafast growth of high-quality triangular WSe_2 domain observed experimentally.[10]

Path 2: fast kink nucleation and ultrafast kink propagation

In Path 2, there are two major steps: the kink nucleation and kink propagation. Since compact edges were observed experimentally,[10] this suggests that the growth rate is likely to be limited by the kink formation, rather than kink propagation. The energy barriers for the kink nucleation are the same as the attachment processes (0.55 eV for zigzag attachment and 0.32 eV for kink formation.[10]). A couple of interesting questions arise: why can the kink propagation be ultrafast? During the kink propagation, where are the feeding atoms coming from? To answer these questions, we carried out detailed analyses and further kMC simulations. Previous first-principles calculations[10] showed that the energy reduction of Se atom from the vapor to deposit to an existing kink site at the growth front is 2.5 eV and the energy reduction of Se

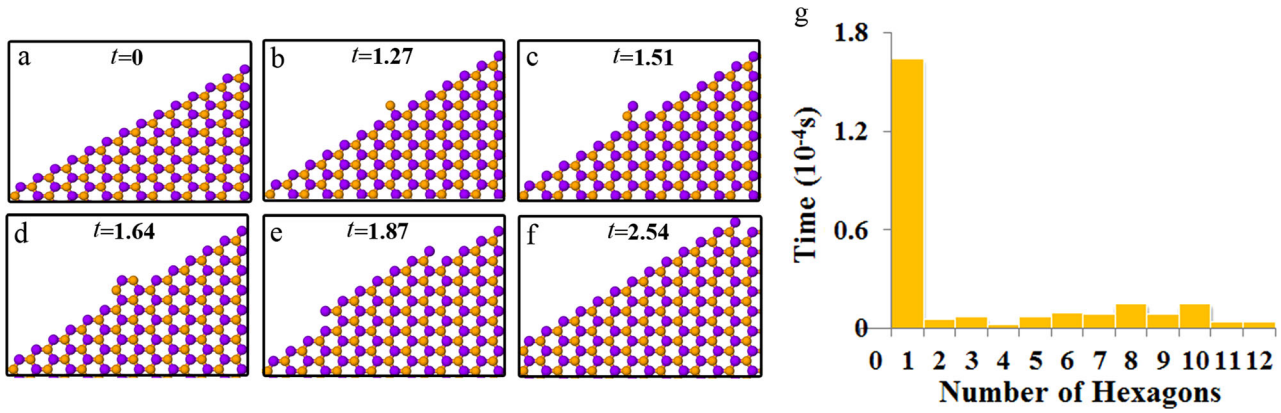

Fig. 3 **a**–**f** Kink nucleation and propagation processes. Purple and orange spheres represent the W and Se, respectively. **g** The estimated formation times for each hexagon during the kink nucleation and propagation at the W-terminated zigzag edge. Time unit: 10^{-4} s

atom from the substrate to attach an existing kink site at the growth front is 1.0 eV. Moreover, the deposition process is barrierless while the attachment of Se atom on the substrate to the kink encounters a barrier of 0.32 eV from first-principles calculations.[10] Therefore, the deposition of atoms directly to the kinks at the edges from the vapor is energetically more favorable than the attachment from the substrate surface. Hence, the ultrafast kink propagation is due to the large energy reduction in the attachment of Se atoms to the existing kink sites, particularly from the vapor.

In Gao et al.[10] experiments, the deposition of Se is the rate-limiting process, and the growth rate increases with increasing the feeding rate of Se. Therefore, the overall flux of W is larger than that of Se, and most domains are of W-terminated zigzag edges. Using the energy barriers from first-principle calculations,[10] we performed kMC simulations on the growth front of W-terminated zigzag edges with $F_W = 2.5 \times 10^{-4}$ ML/s, $F_S = 0.5 \times 10^{-4}$ ML/s, whose growth rate agrees well with Gao et al.[10] experiments. Snapshots in the growth process at the W-terminated zigzag edge are shown in Fig. 3a–f. Initially, Se dimers are attached (from the substrate) or deposited (from the vapor) to the W-terminated zigzag edge (c.f. Fig. 3a, b). For a larger flux of W, W atoms are attached or deposited to bond Se atoms at the edge (c.f. Fig. 3c), generating energetically favorable armchair sites of Se to form a kink. The sites of Se are then occupied by either a diffusing Se dimer or a Se dimer from the vapor phase, resulting in the formation of a hexagonal kink (c.f. Fig. 3d). Then, W atoms will attach, diffuse, or deposit to bond to the kink due to the large flux, bringing in new energetically favorable armchair sites of Se (c.f. Fig. 3e). Finally, these sites of Se are quickly occupied by atoms due to the absence of energy barriers. This repeating process induces an ultrafast propagation of the hexagonal kink (c.f. Fig. 3f). We have also estimated the time to form each hexagon during the formation and propagation of a kink and the results are shown in Fig. 3g. It is seen the time to form the first hexagonal kink is ~1.64×10^{-4} s, which is the longest. The formation times for subsequent hexagons are much shorter, in the range of (0.1×10^{-4} s, 0.2×10^{-4} s). The above simulations demonstrate that once a hexagonal kink is nucleated at the zigzag edge, it will quickly propagate along the edge. The growth rate is limited by the kink nucleation rate, which is related to the attachment rate or the edge deposition from the vapor phase.

Furthermore, Gao et al.[10] observed triangular domains with two opposite orientations in their experiments (c.f. Fig. 4l). Interestingly, Najmaei et al.[54] experimentally not only observed triangular domains with opposite orientations, but also hexagonal domains of MoS_2 at different concentrations of sulfur (c.f. Fig. 4j, k). Their experiments showed that when the sulfur concentration was low, hexagonal domains appeared (c.f. Fig. 4j); while when the sulfur concentration was increased, triangular domains with opposite orientations appeared on the same substrate surfaces (c.f. Fig. 4k). The underlying reason for these different domain shapes and orientations is not yet fully understood.

To understand the formation of these different domain shapes, we performed kMC simulations to investigate the growth of the WSe_2 domain at the three different deposition fluxes of W atoms and Se dimers, that is, $F_W = F_S$, $F_W < F_S$, and $F_W > F_S$. The domain morphologies for these three different growth conditions are shown in Fig. 4a–c, respectively. It is seen that when the deposition fluxes of W atoms and Se dimers are identical ($F_W = F_S = 2.5 \times 10^{-4}$ ML/s), the domain morphology exhibits a compact hexagonal shape (c.f. Fig. 4a and Supplementary Movie 4). When the deposition flux of Se dimers is larger than that of W atoms ($F_W = 0.5 \times 10^{-4}$ ML/s, $F_S = 2.5 \times 10^{-4}$ ML/s), the domain becomes a triangular shape with Se-terminated zigzag edges as shown in Fig. 4b and Supplementary Movie 5. When the deposition flux of W atoms is larger than that of Se dimers ($F_W = 2.5 \times 10^{-4}$ ML/s, $F_S = 0.5 \times 10^{-4}$ ML/s), the domain turns into an opposite-orientated triangular shape with W-terminated zigzag edges (c.f. Fig. 4c and Supplementary Movie 6). In Gao et al. experiment,[10] triangular domains with both W-terminated edge and Se-terminated edge were observed. Therefore, the local fluctuations of W and Se fluxes may be a possible mechanism for observed opposite-oriented triangles. However, the flux at which the triangles grow next to each other may not be very different for W and Se. In that case, the opposite-oriented triangles could be formed by opposite-orientated nuclei with the same type or different types of edges. To verify this, we performed KMC simulations with opposite-orientated nuclei (c.f. Fig. 4b–d). The simulation results suggest that indeed the opposite-orientated domains with the same type or different types of edges can be achieved. Hence, our work suggests two possible approaches to achieve opposite-oriented triangles: (1) different fluxes for W and Se (Fig. 4b vs 4c), and (2) opposite-orientated nuclei (Fig. 4b vs 4d).

The formation of these hexagonal and triangular domains from the initial circular shape can be well understood by using the kinetic Wulff construction theory (c.f. Fig. 4e). Since the domain morphology is governed by the kinetics of attachment and detachment of atoms to the edges, during the growth process, the fast-growing edges eventually lose out to those with the slow-growing edges. During the initial growth, we found that the growth rates of W-terminated and Se-terminated zigzag edges are nearly equal due to the small size of nucleus, which are slower than the armchair edges. Therefore, the domain shape will transform from a circular shape to a hexagonal shape with only zigzag edges. As the domain grows continuously, the zigzag edges become sensitive to the deposition fluxes of Se dimers and W atoms. When the growth rate of Se-terminated zigzag edge is

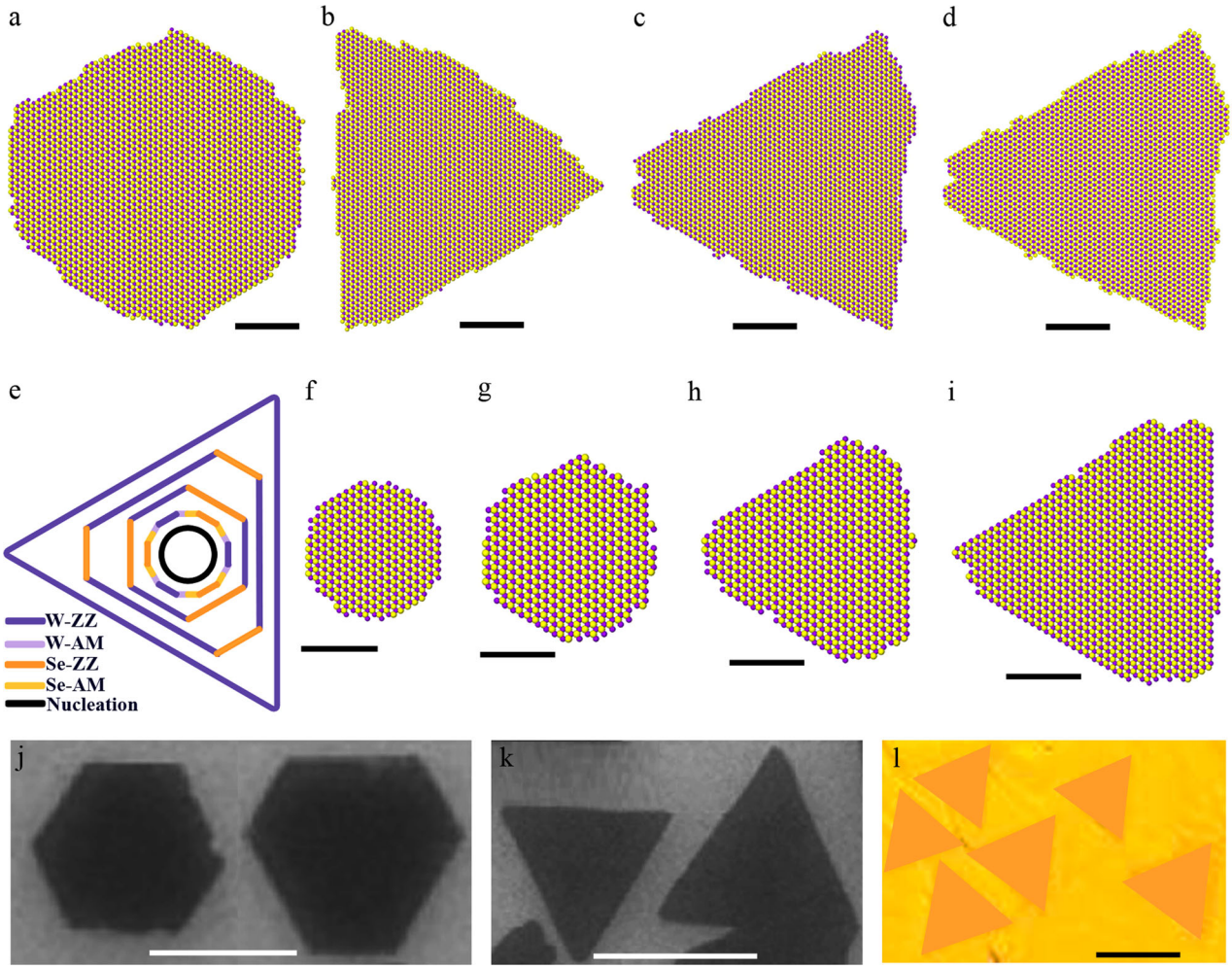

Fig. 4 Snapshots of the WSe_2 domain at 800 °C when **a** $F_W = F_S = 2.5 \times 10^{-4}$ ML/s, **b** $F_W = 0.5 \times 10^{-4}$ ML/s, $F_S = 2.5 \times 10^{-4}$ ML/s, **c** $F_W = 2.5 \times 10^{-4}$ ML/s, $F_S = 0.5 \times 10^{-4}$ ML/s, and **d** $F_W = 0.5 \times 10^{-4}$ ML/s, $F_S = 2.5 \times 10^{-4}$ ML/s. (**a**–**c**) have the same-orientated nuclei, while (**d**) has an opposite-orientated nucleus with (**a**–**c**). **a**–**d** Scale bar: 10*a* ($a = 0.332$ nm). **e** Illustration of the kinetic Wulff construction theory during the domain growth. **f**–**i** Snapshots showing the shape evolution from the initial circular shape to the final triangular shape with W-terminated zigzag edges. W atoms are marked by purple spheres. **f**–**i** Scale bar: 10*a* ($a = 0.332$ nm). Scanning electron microscopy images of MoS_2 at **j** lower sulfur concentrations and **k** higher sulfur concentrations. **j**, **k** Scale bar: 10 μm. **j**, **k** Reproduced from ref. [54] with permission from Springer Nature. **l** Scanning electron microscopy images of WSe_2 in Gao et al. ultrafast growth. **l** Scale bar: 100 μm. **l** Reproduced from ref. [10] with permission from John Wiley and Sons

larger than that of W-terminated zigzag edge, the domain will transform from a hexagonal shape with mixed W-terminated and Se-terminated zigzag edges to a triangular shape with only W-terminated zigzag edges. Conversely, when the growth rate of Se-terminated zigzag edge is smaller than that of W-terminated zigzag edge, the domain morphology will transform from the hexagonal shape with mixed W-terminated and Se-terminated zigzag edges to a triangular shape with only Se-terminated zigzag edges, giving rise to two opposite-oriented triangular shapes. Figure 4f–i shows the evolution of domain morphology during the growth with a larger deposition flux of W. It is seen clearly that the domain morphology transforms from a circular shape to a hexagonal shape initially (c.f. Fig. 4f, g). After that, the domain morphology transforms from a hexagonal shape to a triangular shape with only W-terminated zigzag edges (c.f. Fig. 4g–i), which agrees well with the kinetic Wulff construction theory (c.f. Fig. 4e). It is noted that there were two opposite orientations of triangular domains in experiments.[10,54] The underlying reason could be due to the fluctuations in fluxes at different local regions on the substrate surfaces. In Gao et al. experiments, since the W flux is higher than Se flux, the triangular domains with W-terminated edges are dominant (c.f. Fig. 4l). In some regions, however, the flux of W atoms could be smaller than that of Se atoms due to the flux fluctuations, which might result in domains with Se-terminated zigzag edges. Similarly, the triangular domains with opposite orientations observed in Najmaei et al. experiments[54] might also be formed due to the fluctuations in local fluxes of Mo and S atoms. Of course, the opposite-oriented triangles could also be formed by opposite-orientated nuclei, and these triangles might have the same type or different types of edges.

The fast (~3 μm/s) and ultrafast growth (~60 μm/s) of graphene has already been reported.[27–29] These studies revealed that the supply of oxygen decreased the graphene nucleation density by passivating Cu surface active sites[29] and accelerated graphene domain growth by lowering the energy barrier to the decomposition of carbon feedstock.[28] The graphene domain shape in ultrafast growth rate was often dendrite, hexagonal, or circular,[28,29] but not triangle with compact edges. For the ultrafast growth of WSe_2, although the growth rate was similar (~26 μm/s),[10] the domains are of a triangular shape with compact

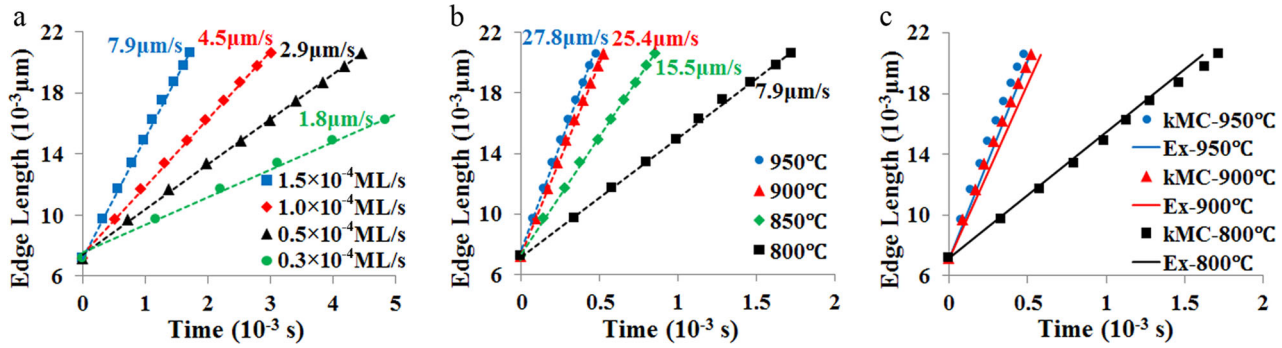

Fig. 5 Comparison of growth rate between our kMC simulations and Gao et al. experiments.[10] **a** Comparison of growth rate at different deposition fluxes: $F_W = 2.5 \times 10^{-4}$ ML/s, $U_S = 1.5 \times 10^{-4}$, 1.0×10^{-4}, 0.5×10^{-4}, and 0.3×10^{-4} ML/s. **b** Comparison of growth rate at growth temperatures: 800, 850, 900, and 950 °C. **c** Comparison of growth rate at different deposition fluxes and temperatures: 800 °C ($F_W = 2.5 \times 10^{-4}$ ML/s, $F_S = 1.5 \times 10^{-4}$ ML/s), and 900 °C ($F_W = 2.5 \times 10^{-4}$ ML/s, $F_S = 1.5 \times 10^{-4}$ ML/s), and 950 °C ($F_W = 2.5 \times 10^{-4}$ ML/s, $F_S = 0.5 \times 10^{-4}$ ML/s) between kMC simulation results (7.9, 25.4, and 27.8 μm/s) and the experimental results (8.3, 23, and 26 μm/s)[10]

edges, indicating a different underlying mechanism from graphene. Our work shows that the ultrafast growth and compact edges of WSe_2 domain result from the fast kink nucleation and ultrafast kink propagation. The fast kink nucleation is due to the lower energy barrier of edge attachment, and the ultrafast kink propagation comes from the ultrafast surface diffusion or direct deposition of W and Se adatoms to the growth front.

Growth rates varying with fluxes and temperatures

In the following, we would like to compare our kMC simulation results with the experimental results obtained by Gao et al.[10] under different growth conditions. We note that Gao et al.[10] reported a drastic increase in the growth rate from 0.26 to 8.3 μm/s with increasing the feeding rate of Se from 1.4 to 65 standard cubic centimeter per minute (sccm) at 800 °C. Our simulation results show almost the same growth rates from 1.8 to 7.9 μm/s as the deposition flux of Se dimer increases (by increasing F_S from 0.3×10^{-4} ML/s to 1.5×10^{-4} ML/s at a constant $F_W = 2.5 \times 10^{-4}$ ML/s) (c.f. Fig. 5a). Gao et al.[10] also reported a sharp increase in the growth rate from 8.3 to 26 μm/s by increasing the temperature from 800 to 950 °C. The growth rate in our simulations increases from 7.9 to 27.8 μm/s with increasing the temperature from 800 to 950 °C (c.f. Fig. 5b). In addition, the growth rates at different deposition fluxes and temperatures from both our kMC simulation results (800 °C: 7.9 μm/s, 900 °C: 25.4 μm/s, and 950 °C: 27.8 μm/s) and the experimental results (800 °C: 8.3 μm/s, 900 °C: 23 μm/s, and 950 °C: 26 μm/s) are shown in Fig. 5c, and a good agreement is evident. These comparisons in the growth rate between the simulations and experiments indicate that there is an almost quantitative agreement between our kMC simulations and the experimental results.

DISCUSSION

By performing growth process analysis, kMC simulations and first-principles calculations, we investigated the underlying mechanism for the ultrafast growth of regular triangular WSe_2 monolayer with compact edges on Au(111) via CVD. Our growth process analysis suggested two possible paths leading to the ultrafast growth of compact triangular domain, that is, Path 1: fast edge attachment and ultrafast edge diffusion, and Path 2: fast kink nucleation and ultrafast kink propagation along the edge. Based on our DFT calculations and comparison with the experimental growth rate and morphology, we ruled out Path 1 due to the high diffusion barriers along the domain edges. Our kMC simulations suggested that Path 2 is the underlying mechanism responsible for the ultrafast growth observed in Gao et al.[10] experiments since the simulated domain morphology, domain orientation, and growth rate are in agreement with the experimental results under wide ranges of deposition flux and temperature. We further showed that in Path 2, kink nucleation is clearly the limiting factor. Hence, the growth rate can be further tuned by controlling the kink nucleation rate, which is in turn controlled by the deposition of atoms from the vapor or by the attachment of the diffusing atoms on the substrate. In addition, the domain orientation can also be regulated by controlling the relative dominance of deposition species. Our work reveals that the fast kink nucleation and ultrafast kink propagation are the underlying mechanisms responsible for the ultrafast growth of WSe_2 domains. The fast kink nucleation is due to the low energy barrier of edge attachment. The ultrafast kink propagation results either from the even lower energy barrier of surface diffusion of adatoms or their direct deposition from vapor to the growth front. This mechanism can be potentially extended to other 2D materials. For example, the ultrafast growth of other TMDs may also be achievable if a substrate is able to greatly enhance the surface diffusion of adatoms or promote their direct deposition from vapor to the growth front.

METHODS

Simulation method

Our kMC simulation model is illustrated in Fig. 1, in which 2D hexagonal WSe_2 lattice (lattice constant $a = 0.332$ nm) is used.[55] An initial circular nucleus of WSe_2 domain with a diameter of 5.3 nm is introduced at the center of the simulation box. All six dominant events discussed above are considered in the model. The energetics for these events was obtained by using first-principles calculations either from lirerature[10] or from our own. To simulate the deposition and diffusion of adatoms on the Au(111) substrate, the substrate surface was mapped into a hexagonal lattice with the same lattice constants of WSe_2. As a result, W and Se will deposit or diffuse on these corresponding lattice sites (on-lattice simulation). However, the energetics will follow these on the Au(111) substrate. To simplify the deposition and diffusion processes, we only consider W atoms and Se dimers in our simulations. The dimensions of the kMC simulation box are taken as 28.2×32.6 nm^2. Periodic boundary conditions are taken along the lateral directions. The details of our kMC model and corresponding energetics are given in Supplementary Information.

DATA AVAILABILITY

The data that support the findings of this study and the code for the strategy proposed in this study are available from the corresponding author upon request.

ACKNOWLEDGEMENTS

The authors gratefully acknowledge the support from the Science and Engineering Research Council through grant (152-70-00017) and use of computing resources at

the A*STAR Computational Resource Centre and National Supercomputer Centre, Singapore. J. Gao also thanks the Start-Up grant of DUT (3005-852069).

AUTHOR CONTRIBUTIONS

Y.-W.Z. supervised and conceived this project. S.C. established the theoretical models and performed kMC simulations. J.G. did first-principles calculations. B.M.S., G.Z., V.S., and R.H. discussed the results. S.C. wrote the paper. All of the authors commented on the manuscript.

ADDITIONAL INFORMATION

Supplementary information accompanies the paper on the *npj Computational Materials* website (https://doi.org/10.1038/s41524-019-0167-2).

Competing interests: The authors declare no competing interests.

Publisher's note: Springer Nature remains neutral with regard to jurisdictional claims in published maps and institutional affiliations.

REFERENCES

1. Liu, Y. et al. Van der Waals heterostructures and devices. *Nat. Rev. Mater.* **1**, 16042 (2016).
2. Lin, L. & Liu, Z. Graphene synthesis: on-the-spot growth. *Nat. Mater.* **15**, 9–10 (2016).
3. Zhu, S. et al. Metallic and highly conducting two-dimensional atomic arrays of sulfur enabled by molybdenum disulfide nanotemplate. *npj Comput. Mater.* **3**, 41 (2017).
4. Xie, G. et al. Ultra-low thermal conductivity of two-dimensional phononic crystals in the incoherent regime. *npj Comput. Mater.* **4**, 21 (2018).
5. Wang, Q. H., Kalantar-Zadeh, K., Kis, A., Coleman, J. N. & Strano, M. S. Electronics and optoelectronics of two-dimensional transition metal dichalcogenides. *Nat. Nanotechnol.* **7**, 699–712 (2012).
6. Reber, A. C. & Khanna, S. N. $C_o6S_e8(PE_t3)6$ superatoms as tunable chemical dopants for two-dimensional semiconductors. *npj Comput. Mater.* **4**, 33 (2018).
7. Duan, X., Wang, C., Pan, A., Yu, R. & Duan, X. Two-dimensional transition metal dichalcogenides as atomically thin semiconductors: opportunities and challenges. *Chem. Soc. Rev.* **44**, 8859–8876 (2015).
8. Terrones, H., Lopez-Urias, F. & Terrones, M. Novel hetero-layered materials with tunable direct band gaps by sandwiching different metal disulfides and diselenides. *Sci. Rep.* **3**, 1549 (2013).
9. Desai, S. B. et al. Strain-induced indirect to direct bandgap transition in multilayer WSe_2. *Nano Lett.* **14**, 4592–4597 (2014).
10. Gao, Y. et al. Ultrafast growth of high-quality monolayer WSe_2 on Au. *Adv. Mater.* **29**, 1700990 (2017).
11. Song, I. et al. Patternable large-scale molybdenium disulfide atomic layers grown by gold-assisted chemical vapor deposition. *Angew. Chem. Int. Ed.* **53**, 1266–1269 (2014).
12. Yun, S. J. et al. Synthesis of centimeter-scale monolayer tungsten disulfide film on gold foils. *ACS Nano* **9**, 5510–5519 (2015).
13. Gao, Y. et al. Large-area synthesis of high-quality and uniform monolayer WS_2 on reusable Au foils. *Nat. Commun.* **6**, 8569 (2015).
14. Koperski, M. et al. Single photon emitters in exfoliated WSe_2 structures. *Nat. Nanotechnol.* **10**, 503 (2015).
15. Liu, W. et al. Role of metal contacts in designing high-performance monolayer n-type WSe_2 field effect transistors. *Nano Lett.* **13**, 1983–1990 (2013).
16. Nicolosi, V., Chhowalla, M., Kanatzidis, M. G., Strano, M. S. & Coleman, J. N. Liquid exfoliation of layered materials. *Science* **340**, 1226419 (2013).
17. Coleman, J. N. et al. Two-dimensional nanosheets produced by liquid exfoliation of layered materials. *Science* **331**, 568–571 (2011).
18. Lee, K. et al. Electrical characteristics of molybdenum disulfide flakes produced by liquid exfoliation. *Adv. Mater.* **23**, 4178–4182 (2011).
19. Eichfeld, S. M. et al. Highly scalable, atomically thin WSe_2 grown via metal–organic chemical vapor deposition. *ACS Nano* **9**, 2080–2087 (2015).
20. Zhou, H. L. et al. Large area growth and electrical properties of p-type WSe_2 atomic layers. *Nano Lett.* **15**, 709–713 (2015).
21. Zhang, C. et al. Strain distributions and their influence on electronic structures of WSe_2–MoS_2 laterally strained heterojunctions. *Nat. Nanotechnol.* **13**, 152 (2018).
22. Huang, C. et al. Lateral heterojunctions within monolayer $MoSe_2$–WSe_2 semiconductors. *Nat. Mater.* **13**, 1096 (2014).
23. Liu, B. et al. Chemical vapor deposition growth of monolayer WSe_2 with tunable device characteristics and growth mechanism study. *ACS Nano* **9**, 6119–6127 (2015).
24. Chen, W. et al. Oxygen-assisted chemical vapor deposition growth of large single-crystal and high-quality monolayer MoS_2. *J. Am. Chem. Soc.* **137**, 15632–15635 (2015).
25. Gong, Y. et al. Synthesis of millimeter-scale transition metal dichalcogenides single crystals. *Adv. Funct. Mater.* **26**, 2009–2015 (2016).
26. Li, S. et al. Halide-assisted atmospheric pressure growth of large WSe_2 and WS_2 monolayer crystals. *Appl. Mater. Today* **1**, 60–66 (2015).
27. Wu, T. et al. Fast growth of inch-sized single-crystalline graphene from a controlled single nucleus on Cu–Ni alloys. *Nat. Mater.* **15**, 43–48 (2016).
28. Xu, X. et al. Ultrafast growth of single-crystal grapheme assisted by a continuous oxygen supply. *Nat. Nanotechnol.* **11**, 930–936 (2016).
29. Hao, Y. et al. The role of surface oxygen in the growth of large single-crystal graphene on copper. *Science* **342**, 720–723 (2013).
30. Artyukhov, V. I., Liu, Y. & Yakobson, B. I. Equilibrium at the edge and atomistic mechanisms of graphene growth. *Proc. Natl Acad. Sci. U.S.A.* **109**, 15136–15140 (2012).
31. Zhang, Z., Liu, Y., Yang, Y. & Yakobson, B. I. Growth mechanism and morphology of hexagonal boron nitride. *Nano Lett.* **16**, 1398–1403 (2016).
32. Shi, J. et al. Controllable growth and transfer of monolayer MoS_2 on Au foils and its potential application in hydrogen evolution reaction. *ACS Nano* **8**, 10196–10204 (2014).
33. Gao, J., Yip, J., Zhao, J., Yakobson, B. I. & Ding, F. Graphene nucleation on transition metal surface: structure transformation and role of the metal step edge. *J. Am. Chem. Soc.* **133**, 5009–5015 (2011).
34. Yuan, Q. et al. Magic carbon clusters in the chemical vapor deposition growth of graphene. *J. Am. Chem. Soc.* **134**, 2970–2975 (2012).
35. Zhang, D. B. & Wei, S. H. Inhomogeneous strain-induced half-metallicity in bent zigzag graphene nanoribbons. *npj Comput. Mater.* **3**, 32 (2017).
36. Gao, J., Xu, Z., Chen, S., Bharathi, M. S. & Zhang, Y.-W. Computational understanding of the growth of 2D materials. *Adv. Theory Simul.* **1**, 1800085 (2018).
37. Gao, J., Zhao, J. & Ding, F. Transition metal surface passivation induced graphene edge reconstruction. *J. Am. Chem. Soc.* **134**, 6204–6209 (2012).
38. Bharathi, M. S. et al. Oxygen-promoted chemical vapor deposition of graphene on copper: a combined modeling and experimental study. *ACS Nano* **12**, 9372–9380 (2018).
39. Chen, S. et al. Unveiling the competitive role of etching in graphene growth during chemical vapor deposition. *2D Mater.* **6**, 015031 (2019).
40. Hao, Y. et al. Oxygen-activated growth and bandgap tunability of large single-crystal bilayer graphene. *Nat. Nanotechnol.* **11**, 426 (2016).
41. Meca, E., Lowengrub, J., Kim, H., Mattevi, C. & Shenoy, V. B. Epitaxial graphene growth and shape dynamics on copper: phase-field modeling and experiments. *Nano Lett.* **13**, 5692–5697 (2013).
42. Ma, T. et al. Edge-controlled growth and kinetics of single-crystal graphene domains by chemical vapor deposition. *Proc. Natl Acad. Sci. U.S.A.* **110**, 20386–20391 (2013).
43. Gao, Y. et al. Ultrahard carbon film from epitaxial two-layer graphene. *Nat. Nanotechnol.* **13**, 133 (2018).
44. Jiang, H. & Hou, Z. Large-scale epitaxial growth kinetics of graphene: a kinetic Monte Carlo study. *J. Chem. Phys.* **143**, 084109 (2015).
45. Tetlow, H. et al. Growth of epitaxial graphene: theory and experiment. *Phys. Rep.* **542**, 195–295 (2014).
46. Zhang, F. et al. Controlled synthesis of 2D transition metal dichalcogenides: from vertical to planar MoS_2. *2D Mater.* **4**, 025029 (2017).
47. Vilá, R. A. et al. Bottom-up synthesis of vertically oriented two-dimensional materials. *2D Mater.* **3**, 041003 (2016).
48. Hong, S. et al. Computational synthesis of MoS_2 layers by reactive molecular dynamics simulations: initial sulfidation of MoO_3 surfaces. *Nano Lett.* **17**, 4866–4872 (2017).
49. Artyukhov, V. I., Hu, Z., Zhang, Z. & Yakobson, B. I. Topochemistry of bowtie- and star-shaped metal dichalcogenide nanoisland formation. *Nano Lett.* **16**, 3696–3702 (2016).
50. Nie, Y. et al. A kinetic Monte Carlo simulation method of Van der Waals epitaxy for atomistic nucleation-growth processes of transition metal dichalcogenides. *Sci. Rep.* **7**, 2977 (2017).
51. Nie, Y. et al. First principles kinetic Monte Carlo study on the growth patterns of WSe_2 monolayer. *2D Mater.* **3**, 025029 (2016).
52. Yue, R. et al. Nucleation and growth of WSe_2: enabling large grain transition metal dichalcogenides. *2D Mater.* **4**, 045019 (2017).
53. Cui, P. et al. Contrasting structural reconstructions, electronic properties, and magnetic orderings along different edges of zigzag transition metal dichalcogenide nanoribbons. *Nano Lett.* **17**, 1097–1101 (2017).
54. Najmaei, S. et al. Vapour phase growth and grain boundary structure of molybdenum disulphide atomic layers. *Nat. Mater.* **12**, 754–759 (2013).

55. Chang, C.-H., Fan, X., Lin, S.-H. & Kuo, J.-L. Orbital analysis of electronic structure and phonon dispersion in MoS_2, $MoSe_2$, WS_2, and WSe_2 monolayers under strain. *Phys. Rev. B* **88**, 195420 (2013).